12th International Symposium on Turbulence and Shear Flow Phenomena (TSFP12)
Osaka, Japan, July 19–22, 2022

GROWING TURBULENT SPOT IN PLANE COUETTE FLOW PROVIDES DISSIMILARITY BETWEEN MOMENTUM AND HEAT TRANSFERS

Koji Fukudome
Department of Mechanical Engineering
Tokyo University of Science
Niijuku 6-3-1, Katsushika-ku, Tokyo 125-8585, Japan
kfukudome@rs.tus.ac.jp

Takahiro Tsukahara
Department of Mechanical Engineering
Tokyo University of Science
Yamazaki 2641, Noda-shi, Chiba 278-8510 Japan
tsuka@rs.tus.ac.jp

Hiroya Mamori
Department of Mechanical and
Intelligent Systems Engineering
The University of Electro-Communications
Chofugaoka 1-5-1, Chofu, Tokyo, 182-8585, Japan
mamori@uec.ac.jp

Makoto Yamamoto
Department of Mechanical Engineering
Tokyo University of Science
Niijuku 6-3-1, Katsushika-ku, Tokyo 125-8585, Japan
yamamoto@rs.tus.ac.jp

ABSTRACT

Direct numerical simulation of a turbulent spot developing in a laminar plane Couette flow was performed to study the dissimilarity between the heat and momentum transfers. The seed of the turbulent spot was a vortex pair, and the initial flow had an absolute similarity state between heat and momentum transfers. The turbulent spot grows gradually in the early stage and rapidly in the latter stage. The effective heat transfer state, which achieves larger heat transfer than momentum transport, was confirmed in the rapidly developing process. The dissimilarity mechanism was investigated by using a FIK identity equation. We clarified that the turbulent contributions in the friction coefficient and the Stanton number provided the effective heat transfer state. The budgets of Reynolds shear stress and heat flux exhibited that the dissimilarity was attributed to the differences in the pressure-strain and dissipation terms, and the difference in the production terms leads to adverse effects on the effective heat transfer. After the developing process, the pressure-strain term causes a decrease of the heat transfer compared to the skin friction.

INTRODUCTION

In turbulent flows, vortical structures enhance heat and mass transfers compared to those in the laminar flow. While this fact often leads a practical advantage for many engineering applications, the promoted momentum transport should result in the disadvantage of increased frictional drag. It is still challenging for us to achieve an effective heat transfer that outweighs a momentum transfer or to intentionally control a dissimilarity between the transfers, because of a similarity between the heat and momentum transfers, as known as the Chilton–Colburn analogy.

Some effective heat-transfer states were demonstrated by providing a certain vortex structure or applying a flow-control technique. Katoh *et al.* (2013) revealed that the spanwise vortices with cyclonic rotation generate a dissimilarity in the plane Poiseuille flow. The dissimilarity due to anti-cyclonic rotation was also recently clarified (Kubo *et al.*, 2021). Yamamoto *et al.* (2013) performed DNS (direct numerical simulation) of a channel flow with wall suction and blowing based on an optimal control theory. Their streamwise-traveling wave of blowing and suction broke the analogy in heat and momentum transfers, obtaining an effective heat transfer. Motoki *et al.* (2018) determined the optimal heat transfer state by using the Euler–Lagrange equations. More recently, the effective heat transfers were reported for a Taylor–Couette flow with the traveling-wave control (Mamori *et al.*, 2021), and for a turbulent flow on a permeable wall (Motoki *et al.*, 2021).

Recently, there have been reports of effective heat transfer in spontaneously intermittent turbulent fields without any flow control. Fukudome *et al.* (2018) found an effective heat transfer in the plane Couette flow at a subcritical Reynolds number, where the flow field was accompanied by a turbulent stripe. The turbulent stripe is a large-scale spatial intermittent pattern of coexisting laminar and turbulent regions (Prigent *et al.*, 2002; Barkley & Tuckerman, 2007; Duguet *et al.*, 2010; Tsukahara *et al.*, 2014; Fukudome & Iida, 2012). The same effective heat transfer is confirmed with helical turbulence in annular Poiseuille flows (Fukuda & Tsukahara, 2020). More recently, we revealed that the effective heat transfer state is also obtained by a growing turbulent spot in the plane Couette flow (Fukudome *et al.*, 2021). However, the generation mechanism of the dissimilarity has not been understood.

In this paper, we have performed DNS of a developing turbulent spot in the laminar plane Couette flow and its passive-scalar thermal field, in order to discuss the dissimilarity between the momentum and heat transfers in the spatially-intermittent turbulent regime. As a seed of the spot, we added a pair of longitudinal vortices (Lundbladh & Johansson, 1991), and the similarity between streamwise velocity and temperature fields was secured at the beginning of the simulation. Then, the dissimilarity mechanism was analyzed by the identity equations for the skin-friction and the heat-transfer coefficients, i.e., the FIK identities (Fukagata *et al.*, 2002; Yamamoto *et al.*, 2013). Furthermore, the budgets of Reynolds shear stress and turbulent heat flux are compared to identify the generation mechanism of the dissimilarity.

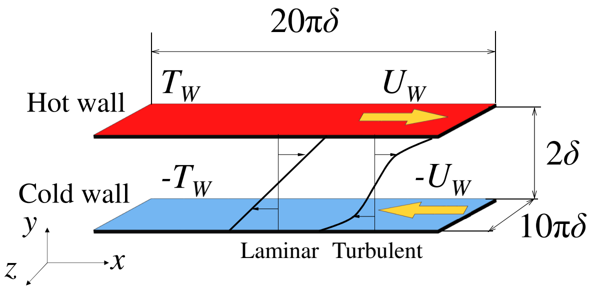

Figure 1. Schematic of target plane Couette flow.

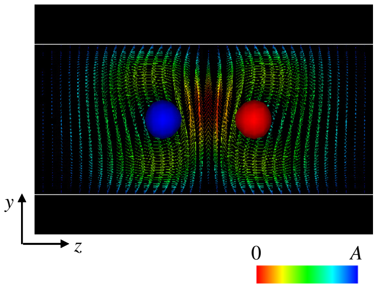

Figure 2. Cross-sectional view of initial disturbance. Red and blue iso-surfaces show vortices identified by the second invariant of the deformation tensor $II^+ = 0.1$ with clockwise and anti-clockwise rotation, respectively. The in-plane velocity vector is colored by its magnitude.

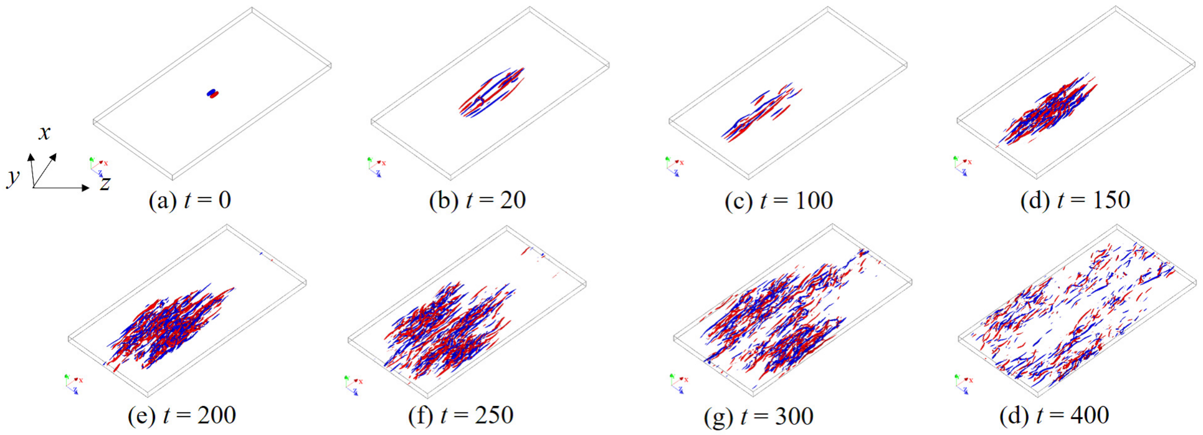

(a) $t = 0$ (b) $t = 20$ (c) $t = 100$ (d) $t = 150$

(e) $t = 200$ (f) $t = 250$ (g) $t = 300$ (d) $t = 400$

Figure 3. Temporal development of the turbulent spot. Red and blue iso-surfaces represent vortical structures identified by the second invariant of the deformation tensor $II^+ = 0.05$ with clockwise and anti-clockwise rotation in streamwise direction, respectively.

NUMERICAL SIMULATION

The flow configuration including the thermal boundary condition is illustrated in Fig. 1, where the periodic boundary conditions are imposed in the streamwise (x) and spanwise (z) directions. The computational domain is $20\pi\delta \times 2\delta \times 10\pi\delta$ and the number of grid points is $256 \times 65 \times 256$, in x, y, and z. The top and bottom walls move at speeds of $+U_W$ and $-U_W$, respectively, and their temperatures are $+T_W$ and $-T_W$, respectively.

The governing equations are the incompressible continuity, Navier–Stokes, and energy equations. The temperature is treated as a passive scalar. For spatial discretization, the spectral method (Kim *et al.*, 1987; Fukudome *et al.*, 2018) is adopted with Fourier series in x and z, and the Chebyshev polynomial expansion in the wall-normal (y) direction. The collocation grid is employed to compute the nonlinear terms in physical space and the grid has 1.5 times finer resolution to remove aliasing errors. As the time integration, the second-order Adams–Bashforth and Crank–Nicolson schemes are adopted for the nonlinear and viscous terms, respectively. Here, the explicit Euler scheme is adopted for the first step of the nonlinear terms to compute from the initial flow field.

The Reynolds and Prandtl numbers are $Re = 450$ and unity, respectively, where Re is based on U_W and δ. The time step size is $\Delta t = 0.01\delta/U_W$. Hereafter, the parameters are normalized by U_W, δ, and/or T_W.

As the initial flow field, we mimic a transient jet from the wall as a single disturbance, introduced by Lundbladh & Johansson (1991). The streamwise velocity and temperature distributions are identical with the laminar value, i.e., $u/U_w = y/\delta$ and $\theta/T_w = y/\delta$, indicating that the initial flow field satisfies the complete similar state between heat and momentum transfers. The stream function Ψ of an initial disturbance is denoted as

$$\Psi = A\left(1-y^2\right)^2 z e^{\left(-x^2-y^2\right)}, \tag{1}$$

where the wall-normal and spanwise velocities can be derived by $v = \partial\Psi/\partial z$ and $w = -\partial\Psi/\partial y$. Here, the parameter A represents the strength of initial disturbance or the peak value of the local wall-normal velocity at the mid of the vortex pair. Figure 2 shows a cross-sectional flow field of the initial disturbance for $A = 1.2$. A pair of counter vortices can be confirmed in the channel center, and the maximum wall-normal velocity at the midpoint of the vortices corresponds to $A = 1.2$.

RESULTS AND DISCUSSION

Figure 3 shows the temporal evolution of the disturbance for $A = 1.2$. At $t = 100$ (Fig. 3(c)), very-extended longitudinal vortical structures composes a spot structure, in which turbulent motions are rather weak yet. Small-scale vortices can be confirmed at $t = 150$ (Fig. 3(d)), then the turbulent spot rapidly grows and it reaches the edge of the computational domain at $t = 300$ (Fig. 3(g)). As reported in the following, our main

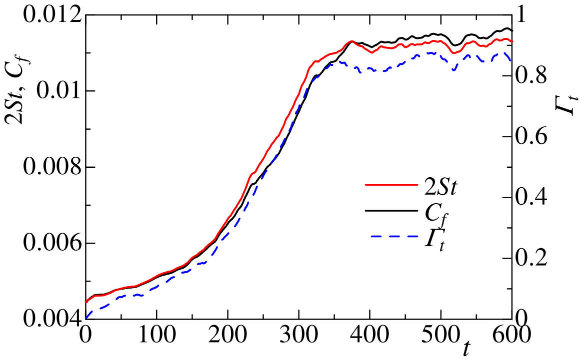

Figure 4. Temporal evolution of St, C_f, and $\mathit{\Gamma}_t$.

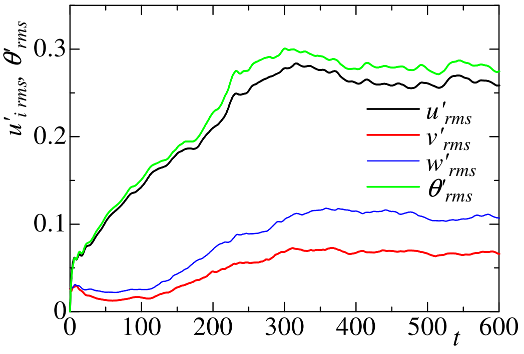

Figure 5. Temporal evolution of RMS values of velocity and temperature fluctuations.

focus is on this spatial-growth period ($t = 150$–300) of the turbulent spot, where an effective heat transfer has been detected.

Figure 4 shows time series of the friction coefficient C_f ($= u_\tau^2/U_W^2$), the Stanton number St ($= h/C_p \rho U_W$), and the intermittent factor $\mathit{\Gamma}_t$, where u_τ, h, C_p, and ρ are the friction velocity, the heat-transfer coefficient, the specific heat, and the density, respectively. The definition of $\mathit{\Gamma}_t$ is the ratio of the turbulent area against the entire channel area, where the turbulent area is identified based on the dissipation rate. The point at which the local dissipation rate averaged in y exceeds half of the average dissipation rate for the entire channel in the instantaneous flow field was determined to be a turbulent region. As shown in Fig. 4, all values gradually increase for $0 < t < 150$ and they rapidly grow for $t > 150$, where the turbulent spot grows spatially and with generating fine-scale eddies inside it. The growth rate of each coefficient during this rapid development process is the largest and constant value. Eventually, they converge at $t \simeq 350$ because the spot size reaches the finite computational domain. Therefore, the turbulent spot grows through the two stages before reaching the domain size: the gradual expansion at the early stage and the rapid expansion at the latter stage. This two-stage growth corresponds to the experiment observation by Tillmark & Alfredsson (1992).

Figure 5 shows the time evolution of the turbulent intensities of velocities and temperature. The fluctuating component is defined by the deviation from the spatially-averaged value at each time instance. Then, the root-mean-square values in the entire channel are obtained irrespective of y. The figure exhibits that the u'_{rms} and θ'_{rms} increase linearly with time. It is interesting to note that θ'_{rms} keeps larger value than u'_{rms}. This is cased by the redistribution between the normal components of Reynolds stresses, resulting in the energy transfer from u' component to the other components. Meanwhile, the v'_{rms} and w'_{rms} are almost constant for $0 < t < 100$, and gradually increase for $100 < t < 350$, implying the spatial growth of "actually turbulent" region with fine-scale eddies.

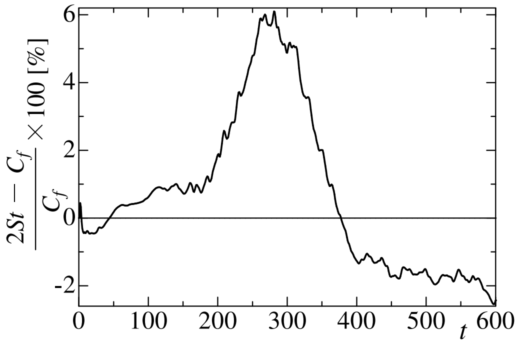

Figure 6. Temporal evolution of the dissimilarity factor.

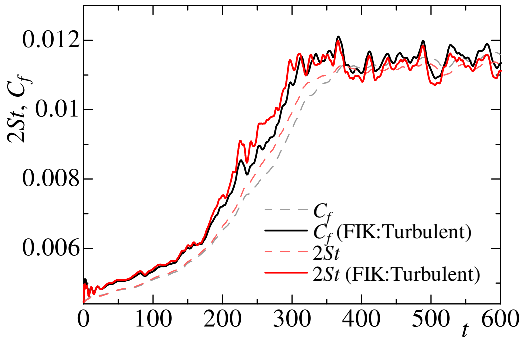

Figure 7. Temporal evolution of the turbulent contribution of FIK identity of St and C_f.

Let us define the dissimilarity factor $(2St - C_f)/C_f$, considering the Chilton–Colburn analogy with $Pr = 1$. Its positive value represents the efficient heat transfer, while its negative does the dominance of frictional drag. The time series of its percentage is plotted in Figure 6. In the period of spatial growth for the spot ($100 < t < 350$), we obtained positive values. In particular, the factor rapidly increases for $175 < t < 250$, and then it turns to decrease. Therefore, the effective heat transfer state ($2St - C_f > 0$) is confirmed for the rapidly growing process of the turbulent spot, until the spot covers the entire domain. When the entire flow field is in a turbulent state ($t > 400$), the factor is negative, which is a tendency known in the literature (Fukudome *et al.*, 2018).

Each of C_f and $2St$ can be decomposed into laminar and turbulent contributions by using FIK identity (Fukagata *et al.*, 2002; Yamamoto *et al.*, 2013). Here, due to the temporal growth of localized turbulence, the unsteady and asymmetric terms (denoted by C_{uv} and $C_{v\theta}$) cannot be ignored, as follows:

$$C_{f\,ave} = \underbrace{\frac{2}{Re}}_{Laminar} + \underbrace{\int_{-1}^{1} \left(-\overline{u'v'}\right) \mathrm{d}y}_{Turbulent} + C_{uv}, \tag{2}$$

$$2St_{ave} = \underbrace{\frac{2}{RePr}}_{Laminar} + \underbrace{\int_{-1}^{1} \left(-\overline{v'\theta'}\right) \mathrm{d}y}_{Turbulent} + C_{v\theta}, \tag{3}$$

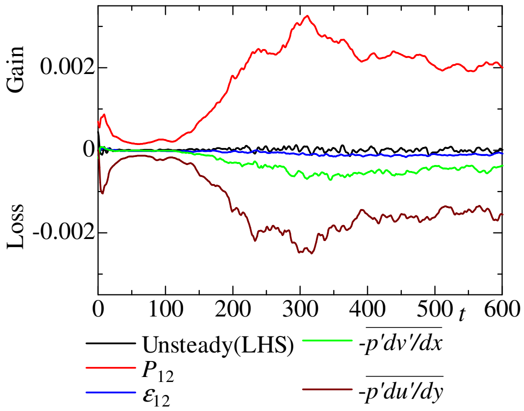

Figure 8. Time evolution of budget for the Reynolds shear stress.

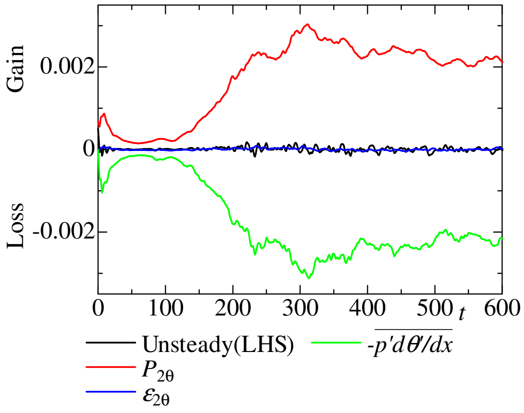

Figure 9. Time evolution of budget for the turbulent heat flux.

where the upper bar shows spatial average in x and z. The laminar contributions are constant at $2/Re$ in both equations, since the present $Pr = 1$. Figure 7 shows the summations of the laminar and turbulent contributions of C_f and $2St$: see the solid lines in the figure. Again, we focus on the spatial-growth period at $t = 150$–300. As the term of $2St$ is larger than the term of C_f, we conjecture that the turbulent contribution produces the effective heat transfer state, i.e., the deviation betweens shear component of Reynolds stresses and turbulent heat flux directly affect the effective hat transfer state.

Finlay, we discuss the transport equations of the Reynolds shear stress $-\overline{u'v'}$ and the turbulent heart flux $-\overline{u'\theta'}$. By averaging in the entire channel (i.e., averaging not only in x and z, but also in y), represented by angle blankets $\langle\rangle$, the diffusion terms are discarded. The transport equations are denoted as

$$\frac{\mathrm{D}\langle -u'v'\rangle}{\mathrm{D}t} = \langle P_{12}\rangle + \langle \varepsilon_{12}\rangle + \langle \Phi_{12}\rangle, \qquad (4)$$

$$P_{12} = \overline{v'v'}\frac{\partial U}{\partial y} + \overline{u'v'}\frac{\partial V}{\partial y}$$

$$\varepsilon_{12} = \frac{2}{Re}\left(\overline{\frac{\partial u'}{\partial x}\frac{\partial v'}{\partial x}} + \overline{\frac{\partial u'}{\partial y}\frac{\partial v'}{\partial y}} + \overline{\frac{\partial u'}{\partial z}\frac{\partial v'}{\partial z}}\right)$$

$$\Phi_{12} = -\overline{p'\left(\frac{\partial v'}{\partial x} + \frac{\partial u'}{\partial y}\right)}$$

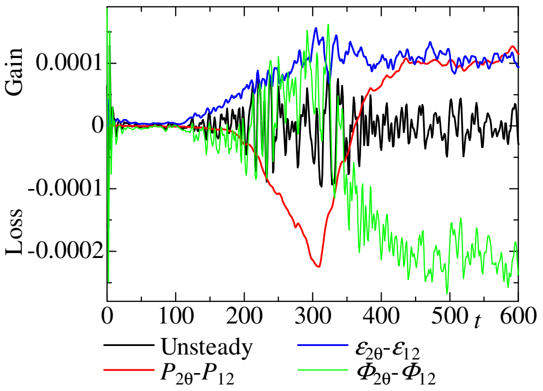

Figure 10. Time evolution of the differences between shear component of Reynolds stresses and turbulent heat flux budget terms.

$$\frac{\mathrm{D}\langle -v'\theta'\rangle}{\mathrm{D}t} = \langle P_{2\theta}\rangle + \langle \varepsilon_{2\theta}\rangle + \langle \Phi_{2\theta}\rangle, \qquad (5)$$

$$P_{2\theta} = \overline{v'v'}\frac{\partial \Theta}{\partial y} + \overline{u'\theta'}\frac{\partial V}{\partial y}$$

$$\varepsilon_{2\theta} = \left(\frac{1}{Re} + \frac{1}{RePr}\right)\left(\overline{\frac{\partial v'}{\partial x}\frac{\partial \theta'}{\partial x}} + \overline{\frac{\partial v'}{\partial y}\frac{\partial \theta'}{\partial y}} + \overline{\frac{\partial v'}{\partial z}\frac{\partial \theta'}{\partial z}}\right)$$

$$\Phi_{2\theta} = -\overline{p'\left(\frac{\partial \theta'}{\partial y}\right)}$$

where P_{12} and $P_{2\theta}$ are production terms, ε_{12} and $\varepsilon_{2\theta}$ are dissipation terms, Φ_{12} and $\Phi_{2\theta}$ are pressure-strain terms, and p is pressure.

Figures 8 and 9 represent temporal evolution of the budget terms for Reynolds shear stress and turbulent heat flux, respectively. The production and pressure-strain terms become larger than the unsteady and dissipation terms. The production terms show similar time evolution; however, P_{12} marks a slightly larger value than $P_{2\theta}$. The pressure-strain terms mark negative values, and the term of $-\overline{p'\partial u'/\partial x}$ shows a smaller value than $-\overline{p'\partial\theta'/\partial x}$ in spite of considerable similarity between u' and θ'. The summation of both pressure-strain terms for the Reynolds shear stress is comparable to the pressure-strain term of turbulent heat flux.

Figure 10 represents the differences in each budget term between the shear component of Reynolds stresses and the turbulent heat flux. For the gradually-growth period ($t < 150$), the dissipation and the pressure-strain term take positive and negative values, respectively. For the spatial-growth period ($t = 150$–300), the dissipation and the production term show positive and negative values, respectively. The pressure-strain term oscillates and the net value shows positive for the spatial-growth period. On the other hand, after the developing process for $t > 350$ (i.e., fully-turbulent state), the pressure-strain term leads to a decrease in heat transfer compared to the friction, while the production and dissipation show the adverse effect of the dissimilarity where the friction outweighs the heat transfer.

CONCLUSION

We performed a direct numerical simulation of a spectral method to study the dissimilarity between momentum and heat transfers for a developing turbulent spot generated by the pair vortices. We obtained the following conclusions.

The obtained turbulent spot grows via two stages: gradually and rapidly growth periods. For the gradual-growth period, the longitudinal vortices extending in the flow direction dominate. For the rapid growth period, which is called also as the spatial-growth period, fine vortices are generated in the turbulent spot and exhibits a linear spatial growth of the spot. In this second stage, an effective heat transfer state is confirmed. The FIK identity revealed that the dissimilarity is mainly caused by the turbulent contributions owing to the Reynolds shear stress and turbulent heat flux. In addition, the difference between the Reynolds shear stress and the turbulent heat flux is found in their dissipation and pressure-strain terms, and their production terms show the adverse effect on the effective heat transfer. For the fully-developed turbulent state, effective heat transfer is prevented by the pressure-strain terms.

ACKNOWLEDGEMENT

K.F. acknowledges the support of the Grant-in-Aid for Early-Career Scientists (No. 20K14671), and T.T. acknowledges the supports of the Grant-in-Aid for Scientific Research (B) (No. 19H02071) by Ministry of Education, Culture, Sports, Science and Technology of Japan.

REFERENCES

Barkley, D. & Tuckerman, L. S. 2007 Mean flow of turbulent–laminar patterns in plane couette flow. *Journal of Fluid Mechanics* **576**, 109–137.

Duguet, Y., Schlatter, P. & Henningson, D. S. 2010 Formation of turbulent patterns near the onset of transition in plane couette flow. *Journal of Fluid Mechanics* **650**, 119–129.

Fukagata, K., Iwamoto, K. & Kasagi, N. 2002 Contribution of reynolds stress distribution to the skin friction in wall-bounded flows. *Physics of Fluids* **14** (11), L73–L76.

Fukuda, T. & Tsukahara, T. 2020 Heat transfer of transitional regime with helical turbulence in annular flow. *International Journal of Heat and Fluid Flow* **82**, 108555.

Fukudome, Koji & Iida, Oaki 2012 Large-scale flow structure in turbulent poiseuille flows at low-reynolds numbers. *Journal of Fluid Science and Technology* **7** (1), 181–195.

Fukudome, K., Tsukahara, T., Mamori, H. & Yamamoto, M. 2021 Emergence of transport dissimilarity by growing turbulent spot in plane couette flow. In *25th Int. Congress of Theor. Appl. Mech. (ICTAM2020+1)*, pp. 1323–1324. Begel House Inc.

Fukudome, K., Tsukahara, T. & Ogami, Y. 2018 Heat and momentum transfer of turbulent stripe in transitional-regime plane couette flow. *International Journal of Advances in Engineering Sciences and Applied Mathematics* **10** (4), 291–298.

Katoh, K., Sakai, A., Fujii, R., Wakimoto, T. & Kawahara, G. 2013 Influence of spanwise vorticity on dissimilarity between turbulent momentum and heat transfer (in japanese). *Transactions of the Japan Society of Mechanical Engineers. B.* **79** (806), 2019–2029.

Kim, J., Moin, P. & Moser, R. 1987 Turbulence statistics in fully developed channel flow at low reynolds number. *Journal of fluid mechanics* **177**, 133–166.

Kubo, A, Kawahara, G & Shimizu, M 2021 Dissimilar heat transfer enhancement by introduction of a vortex tube in plane couette flow. *Fluid Dynamics Research* **53** (1), 015511.

Lundbladh, A. & Johansson, A. V. 1991 Direct simulation of turbulent spots in plane couette flow. *Journal of Fluid Mechanics* **229**, 499–516.

Mamori, H., Fukudome, K., Ogino, K., Fukushima, N. & Yamamoto, M. 2021 Heat transfer enhancement and torque reduction by traveling wave-like blowing and suction in turbulent taylor-couette flow. *Journal of Thermal Science and Technology* **16** (1), JTST0003.

Motoki, S., Kawahara, G. & Shimizu, M. 2018 Optimal heat transfer enhancement in plane couette flow. *Journal of Fluid Mechanics* **835**, 1157–1198.

Motoki, S., Tsugawa, K., Shimizu, M. & Kawahara, G. 2021 The ultimate state of turbulent permeable-channel flow. *arXiv preprint arXiv:2106.07844* .

Prigent, A., Grégoire, G., Chaté, H., Dauchot, O. & van Saarloos, W. 2002 Large-scale finite-wavelength modulation within turbulent shear flows. *Physical review letters* **89** (1), 014501.

Tillmark, N. & Alfredsson, P. H. 1992 Experiments on transition in plane couette flow. *Journal of Fluid Mechanics* **235**, 89–102.

Tsukahara, T., Kawaguchi, Y. & Kawamura, H. 2014 An experimental study on turbulent-stripe structure in transitional channel flow. *arXiv preprint arXiv:1406.1378* .

Yamamoto, A., Hasegawa, Y. & Kasagi, N. 2013 Optimal control of dissimilar heat and momentum transfer in a fully developed turbulent channel flow. *Journal of Fluid Mechanics* **733**, 189–220.